Supercritical deposition of mono- and bimetallic Pd and Pt on TiO_2 coated additively manufactured substrates for the application in the direct synthesis of hydrogen peroxide

Laura L. Trinkies [a,*], Marlene Crone [b], Michael Türk [b], Manfred Kraut [a], Roland Dittmeyer [a]

[a] Institute for Micro Process Engineering - Karlsruhe Institute of Technology, Hermann-von-Helmholtz-Platz, 1, Eggenstein-Leopoldshafen, 76344, Germany
[b] Institute for Technical Thermodynamics and Refrigeration - Karlsruhe Institute of Technology, Kaiserstrasse 12, Karlsruhe, 76128, Germany

ARTICLE INFO

Keywords:
Supercritical fluid
Palladium
Platinum
Mono- and bimetallic
Nanoparticle
Catalyst
Coating
Liquid phase reaction

ABSTRACT

In this study we investigated the properties of mono- and bimetallic Pd and Pt deposited via supercritical fluid reactive deposition (SFRD) on TiO_2 coated additively manufactured substrates. The focus of this work lies on the suitability of these catalysts for the direct synthesis of H_2O_2 in the liquid phase. All catalysts produced showed a high activity towards the desired reaction, derived from high productivities towards the desired product. Thereby, the productivity of the different catalysts decreased in the following order: Pd = PdPt > Pt. In agreement with literature, an increase of the Pd loading from 1 to 2 wt.-% led to a decrease in the productivity. Resulting from comparison with productivities from literature, this method indicates a high suitability of the SFRD method for the suggested application. Due to the easy and eco-friendly nature of this deposition method the catalyst production process can be intensified.

1. Introduction

Being a highly active, green oxidising agent, H_2O_2 is getting more and more attention in sectors as paper and pulp industries, sewage treatment and disinfection applications, as the reprocessing of clinical masks [1,2]. Especially the latter became important during the COVID-19 pandemic [3,4]. Because of the risks associated with the transport of highly concentrated H_2O_2 and the resulting high costs, a decentralised production route is desirable [1,5,6]. Thus, an alternative to the current main production process, the anthraquinone auto-oxidation reaction [7], which is only economically feasible on larger scale [1,8], is of interest. The direct synthesis of H_2O_2 from its elements in a liquid solvent presents an interesting approach. Platinum and palladium, supported on TiO_2 or Al_2O_3, have been studied as catalysts active to the reaction [9]. Unfortunately, noble metal catalysts also catalyse the unwanted side reactions, namely the water formation ($H_2 + {}^1/_2 O_2 \rightarrow H_2O$), the succeeding decomposition of the formed H_2O_2 ($H_2O_2 \rightarrow H_2O + {}^1/_2 O_2$) and the hydrogenation of the same ($H_2O_2 + H_2 \rightarrow 2\,H_2O$). Hence, a lot of research focuses on the development of suitable catalytic systems, which are more selective to the actual H_2O_2-synthesis ($H_2 + O_2 \rightarrow H_2O_2$). Currently, the reaction is often performed in fixed bed or slurry (micro)reactors [10–13]. However, the reaction over catalytically loaded substrates would eliminate the need for cost and energy intensive post-reaction filtering while avoiding additional pressure loss over the reaction zone [14], as it is often found in the cases of the aforementioned reactor concepts.

In this work we present our approach to deposit highly dispersed Pd and Pt from organometallic precursors from supercritical solutions on TiO_2 coated metallic substrates (hereinafter referred to as "substrate"), a process known as supercritical fluid reactive deposition (SFRD). For the first time, we used the reactive deposition of noble metals from supercritical CO_2 to produce structured catalysts for the direct synthesis of H_2O_2.

Supercritical CO_2 ($scCO_2$) is particularly attractive due to its low critical temperature, (304.2 K) and critical pressure (7.39 MPa) and also because it is abundant, cheap, nonflammable and non-toxic [15]. In the supercritical (sc) region, only one homogeneous phase exists due to absence of phase boundaries. In this domain, the thermophysical properties (e.g. density, diffusivity, viscosity) become adjustable between the gas- and liquid-like values. In brief, supercritical fluids have liquid-like densities, gaslike viscosities and kinematic viscosities, and much higher diffusivities than liquids. The low kinematic viscosity corresponds to a high fluidity, which is important for various applications in materials processing due to the fact that natural convection effects are inversely proportional to the square of the kinematic viscosity [16]. In addition, the absence of the surface tension favours an effective nano structuration of complex pore architectures [17]. Furthermore, due to

* Corresponding author.
E-mail address: laura.trinkies@kit.edu (L.L. Trinkies).

Table 1
Selected properties of the substances and chemicals used in the experiments.

Substance	Molar mass g mol^{-1}	Metal content %	Purity %	Supplier –
$Pd(acac)_2$	304.62	34.9	98	abcr GmbH
$Pt(cod)me_2$	333.34	58.5	99	abcr GmbH
CO_2	44.01	–	99.995	Air liquide
H_2	2.02	–	99.9990	Air liquide
TiO_2 (P25)	79.87	–	99.5	Evonik Ind.
Chemicals			Purity %	Supplier –
HNO_3			99	Carl Roth
EtOH			99.88	VWR chemicals
H_2O			DI Milli-Q®	Merck
H_2SO_4			95–98	Sigma Aldrich
NaBr			99	Merck

the complete miscibility of $scCO_2$ with both the gaseous reactants, e.g. H_2 and the reaction products, no liquid byproducts are generated and thus a solvent free product is obtained without extensive thermal or mechanical treatment [18]. Thus, the SFRD process provides an easy and eco-friendly method to deposit metallic nanoparticles with narrow size distributions and controllable metal contents on various substrates.

Examples for successful applications of SFRD process and a survey of the results obtained are given by Siril and Türk [16], by Erkey and Türk [18,19] and recently by Yousefzadeh et al. [20].

First, we outline our method for the deposition of Pd and Pt on TiO_2-coated metal substrates using organometallic precursors and $scCO_2$. Furthermore, we demonstrate that metal nanoparticles deposited via SFRD on substrates exhibit considerable catalytic activity in a liquid phase reaction, i.e. the direct synthesis reaction of H_2O_2. First, we compare the properties of the Pd, Pt and PdPt loaded substrates (hereinafter referred to as "catalysts") resulting from SFRD. We then address the impact of different characteristics of the catalysts, namely the metal type and the metal loading, with respect to the productivity of the catalysts towards the H_2O_2 direct synthesis reaction serving as a measure for the activity of the catalyst.

2. Materials and methods

Table 1 summarises the properties and suppliers of the materials and substances used in this work.

2.1. Precursors used for SFRD

Palladium(II)acetylacetonate ($Pd(acac)_2$) and dimethyl(1,5-cyclooctadiene)-platinum(II) ($Pt(cod)me_2$) were used as organometallic precursors. Although literature frequently refers to improved solubility of organometallic precursors with fluorinated alkyl groups [21–23], the unfluorinated variant, $Pd(acac)_2$, was used, since the formation of a liquid Palladium(II)-hexafluoroacetylacetonate ($Pd(hfac)_2$) phase already occurs at the chosen process conditions [24]. Earlier investigations show that the formation of the liquid phase causes coalescence of the precursor molecules on the substrate, leading to larger metal particles after reduction and thus affecting the dispersion of the metal particles on the substrate and therewith to a lower activity of the catalyst, recognisable by the lower productivities observed. Due to the high solubility in $scCO_2$ and the fact that a solid–fluid equilibrium exists at the chosen process conditions, $Pt(cod)me_2$ was selected as precursor for the synthesis of Pt and PdPt nanoparticles [25].

2.2. Preparation of the additively manufactured stainless steel substrates

The structures chosen as carrier for the supported catalyst are so-called fluid guiding elements (FGE). These threedimensional structures from freeform surfaces are composed of axially and radially arranged fluid guiding blades (FGB), which are connected by plane, tubular segments, the intermediate segments (ISE), see Fig. 1(a). FGB and ISE together form a fluid guiding unit (FGU), as visualised in Fig. 1(b). The FGE thus is made up of several FGU. The detailed working principle of the inserts is described by Hansjosten et al. in [26]. Fig. 1(c) shows the described geometry in a schematic drawing.

Because of their complex structure, the depicted geometries cannot be fabricated by classical, subtractive manufacturing methods. Therefore, the elements used in this work were 3D-printed from stainless steel powder (1.4404, Carpenter Additive) using the powder bed fusion process of metals on a laser based system (PBF-LB/M) on a Realizer SLM 125 (DMG Mori) machine. The laser scanning strategy was adapted so that only the contour lines of the walls of the desired structure were exposed to laser power.

2.3. Catalyst preparation

2.3.1. Coating of the FGE with titanium dioxide

In a first step, a layer of titanium dioxide (TiO_2) was applied to all metallic substrates via an electrophoretic deposition process. Because stainless steel is decomposing H_2O_2, all printed structures were passivated using nitric acid (HNO_3) [28] and rinsed thoroughly afterwards with DI-water before the TiO_2 deposition process.

For the deposition of the TiO_2, the FGE were placed in a glass beaker in which an aluminium foil of the same height as the FGE was rolled and which was filled with a solution of 2 g TiO_2 dispersed in 200 mL of ethanol (EtOH). A voltage of 50 V was applied via an external voltage source (FGE = cathode; aluminium foil = anode) for 5 min. After a short dripping phase under atmospheric conditions, the coatings were calcined at 623 K for 1 h in a muffle furnace.

2.3.2. Supercritical fluid reactive deposition of noble metals

In a typical SFRD experiment, a certain amount of the precursor, either $Pd(acac)_2$ or $Pt(cod)me_2$ and the TiO_2 coated metallic substrate were placed inside the high-pressure vessel (50 mL). Then, gaseous CO_2 was filled into the reactor and heated to the desired temperature within less than 2 h. For improved mixing a magnetic stirrer was deposited in the high pressure vessel. Subsequently, the system was treated in $scCO_2$ at 15.6 MPa and 353 K for 20 h. During this time the organometallic precursor is dissolved in CO_2 and molecular adsorption of the precursor on the substrate takes place. Afterwards, H_2 (12 mol%) was added to the system and the mixture was kept at 15.6 MPa and 353 K for additional 2 h. In this process step, the organometallic precursor is converted to its metal form. At the end of the SFRD experiment, the system is slowly depressurised and cooled down to ambient conditions. Usually two approaches are used for the synthesis of bimetallic NPs via SFRD: simultaneous or sequential deposition. In sequential SFRD, the process described above is applied twice with one precursor at a time. In opposite thereto, in simultaneous SFRD, both precursors are introduced together into the high-pressure vessel, thus simultaneously dissolved in $scCO_2$, and simultaneously adsorbed onto the substrate. Subsequently, both precursors are converted to metallic NPs by means of H_2. Due to the complete miscibility of $scCO_2$ with both the gaseous reactants, e.g. H_2, and the reaction products, no liquid waste is generated and solvent residues on the substrate are completely avoided.

In the current study, the bimetallic PdPt deposition was performed in a simultaneously manner. More details about the SFRD technique and the experimental procedure are published elsewhere [16,18,19]. The appropriate process conditions for the SFRD experiments were derived from experimental studies on the high pressure phase behaviour of the binary systems CO_2/$Pd(acac)_2$ and CO_2/$Pt(cod)me_2$ [24,25].

Fig. 2(a) shows an example of the substrate holder with mounted substrate, i.e. FGE coated with TiO_2, while Fig. 2(b) displays the Pd loaded substrate.

In the following, the metal loaded substrates are labelled according to their total target metal loading. Thus, "CAT-Pd_1" stands for the

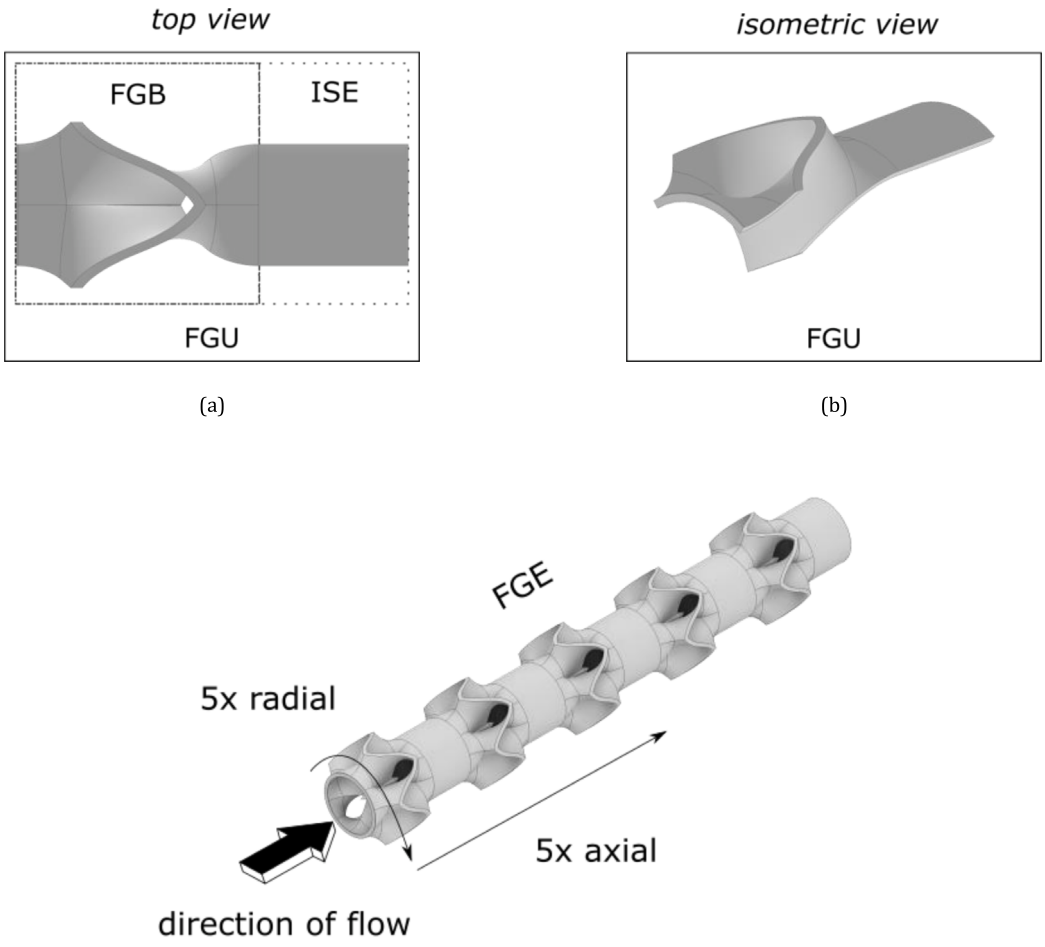

Fig. 1. FGE-geometry: top view of the composition of a FGU from FGB and ISE (a), isometric view of a FGU (b) and composed FGE with five axial and radial FGU each with the direction of flow marked by an arrow (c).
Source: Adapted from [27].

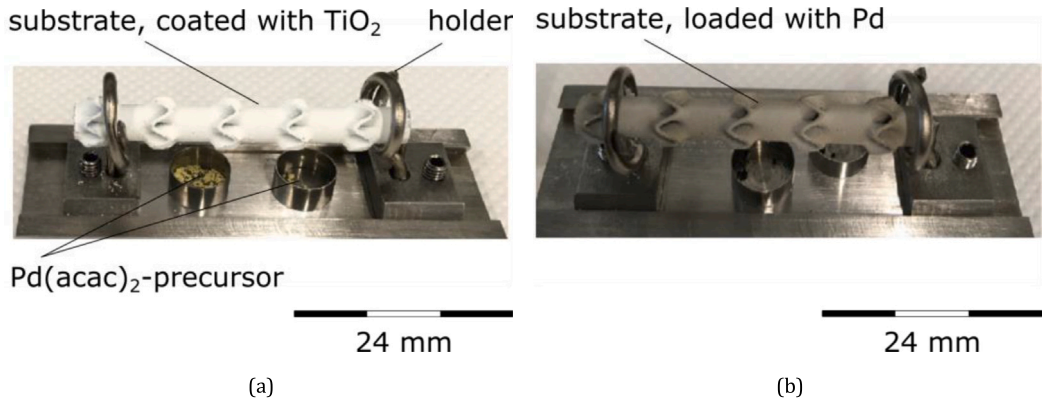

Fig. 2. Substrate before (a) and after (b) SFRD.

substrate loaded with a target loading of 1 wt.-% Pd, "CAT-Pd_2" stands for the substrate loaded with a target loading of 2 wt.-% Pd, "CAT-Pt_1" stands for the substrate loaded with a target loading of 1 wt.-% Pt and "CAT-PdPt_1" stands for the substrate loaded with a target loading of 1 wt.-% PdPt.

2.4. Catalyst characterisation

Particle size. Transmission electron microscopy (TEM) images (FEI Osiris ChemiStern) of the catalysts were used to determine the particle size distribution (PSD). As a rule, about 1000 particle diameters were

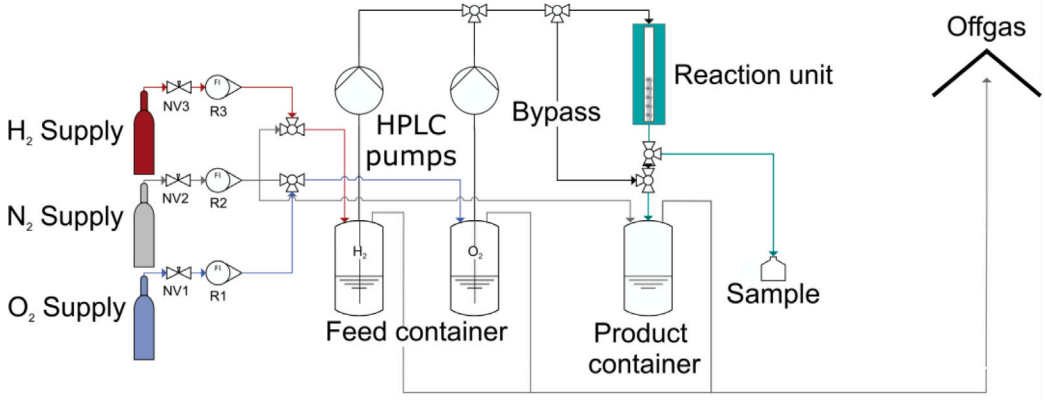

Fig. 3. Experimental set-up for the synthesis measurements to investigate the activity of the catalysts as process flow diagram. *Source:* Adapted from [27].

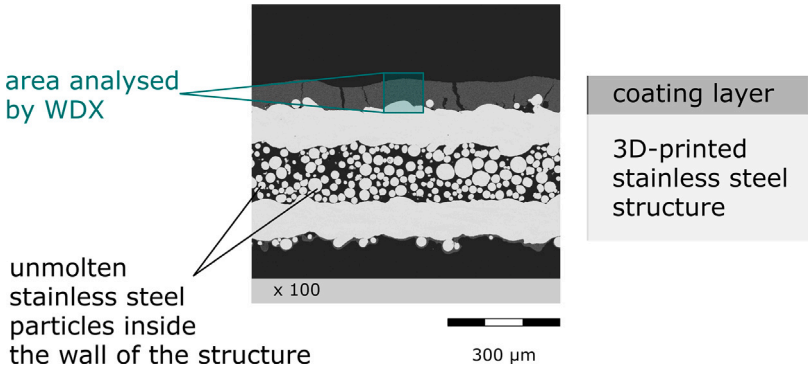

Fig. 4. SEM image of the cross-section of CAT-Pt_1 with a magnification of one hundred. The green rectangle marks the position at which the WDX analysis has been conducted for this sample.

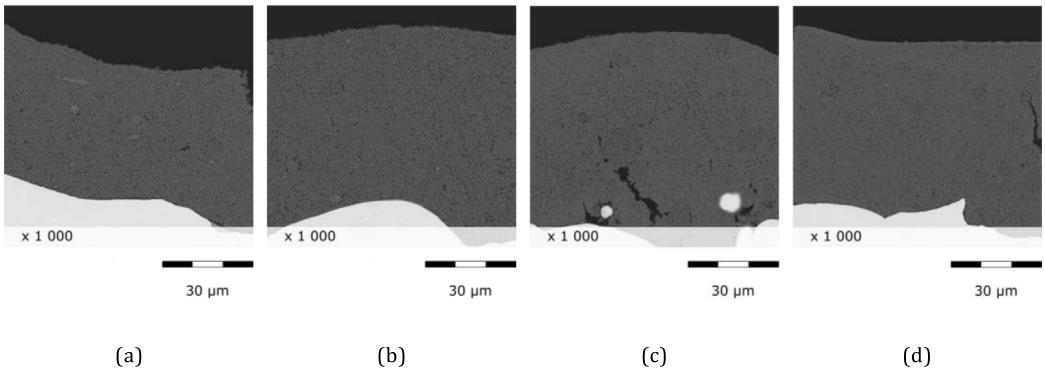

Fig. 5. SEM images of the cross-section of the different catalysts: CAT-Pd_1 (a), CAT-Pt_1 (b), CAT-PdPt_1 (c) and CAT-Pd_2 (d).

considered for the determination of each PSD. Thereby the software ImageJ, version 1.53t, was used.

Catalyst structure. Scanning electron microscopy (SEM) and wavelength-dispersive X-ray spectroscopy (WDX) (JXA 8530F, JOEL) were used to investigate the distribution of the metallic nanoparticles on the substrate and the characterisation of the cross-section of the catalyst, respectively. Furthermore, the bimetallic NPs were analysed by electron dispersive X-ray spectroscopy (EDXS) (FEI Osiris ChemiStern) in line scans of single particles which pass through the centre of the particle.

Reactor setup. The reaction test rig first presented in [29] was adapted for the measurements in this study to the configuration shown in Fig. 3 and the original micro fixed-bed reactor was replaced by a tubular reactor in which the catalysts were inserted. The setup was chosen, because the reactants can be dosed bubble-free and thus equimolar reactant ratios are possible without the need for further dilution by an inert gas. A detailed description of the setup can be found in [27].

Briefly, the solvent in each feed container can be saturated with the respective reactant and streams of the two feeds are combined before entering the reaction unit. For safety reasons, all containers can be flushed with inert gaseous N_2. Samples of the product containing solvent can be taken via the tap after the reaction unit for further analysis of the H_2O_2 by UV–vis spectroscopy using titanium(IV) oxysulfate containing solutions, as described in [30] and similar to the procedure presented in [27].

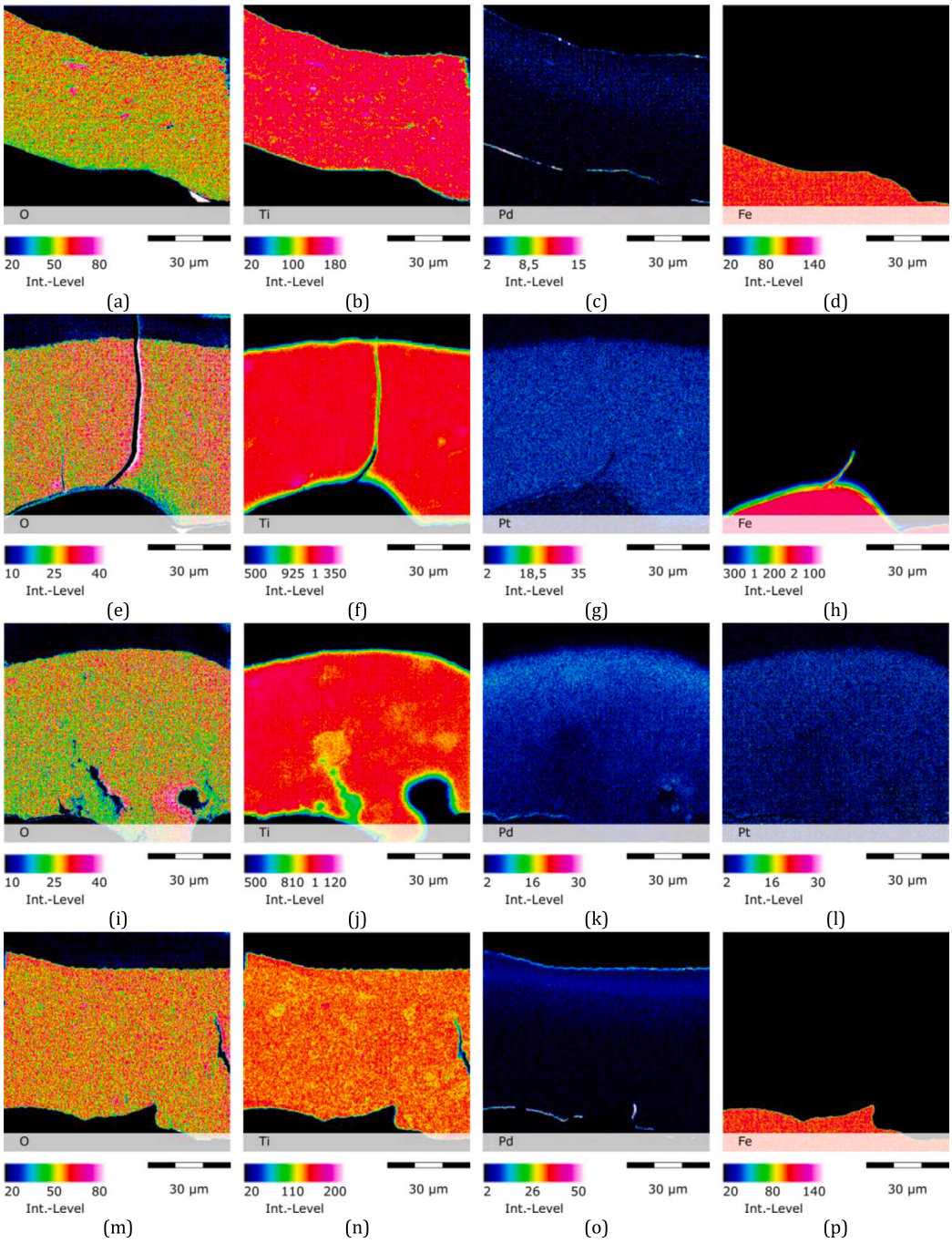

Fig. 6. WDX analysis of the cross-section of CAT-Pd_1 ((a)–(d)), CAT-Pt_1 ((e)–(h)), CAT-PdPt_1 ((i)–(l)) and CAT-Pd_2 ((m)–(p)): distribution of O_2, Ti, Pd/Pt and Fe as indicated by the colour intensity by the colour bar.

Productivity. The reactive behaviour of the catalysts is assessed via the overall synthesis productivity derived by the measured H_2O_2 concentrations after the exposure of the catalysts to reaction conditions. The productivity is defined by the product concentration $c_{H_2O_2}$, the volume flow rate $\dot{V}_L$ and the mass of the respective metal m_{metal}, as given in Eq. (1). Operational instabilities and concentration measurement deviations are taken into account by using the mean productivity calculated by the weighted averaged mean with the corresponding standard deviations.

$$\text{productivity}_{\text{synthesis}} = \frac{c_{H_2O_2} \cdot \dot{V}_L}{m_{\text{metal}}} \tag{1}$$

Experimental procedure. Because the tubing between the feed containers and sampling tap were made of stainless steel, which is active to H_2O_2 decomposition, all components were also passivated with HNO_3 prior to use following the passivation procedure described in [28].

In preparation for the actual experiment, the gaseous reactants were bubbled into the solvent ($H_2O + 0.15\,\text{mmol}\,L^{-1}$ $H_2SO_4 + 4\,\text{mmol}\,L^{-1}$ NaBr) in the two separate feed containers for two hours to fully saturate it with the respective gas. To ensure standardised conditions of the catalysts, H_2 saturated solvent (flow rate: $\dot{V}_L = 5\,\text{mL min}^{-1}$) was led through the reaction unit containing the catalyst for 30 min before the start of each experiment. The feed was then switched in order to start the actual reaction. Therefore, the O_2 and H_2-saturated streams were combined in an equimolar ratio and a total flow rate of $\dot{V}_L = 5\,\text{mL min}^{-1}$ was set in our experiments. Samples of 50 mL were taken each hour and stored in a cool and dark place for later UV–vis-analysis. The validity of

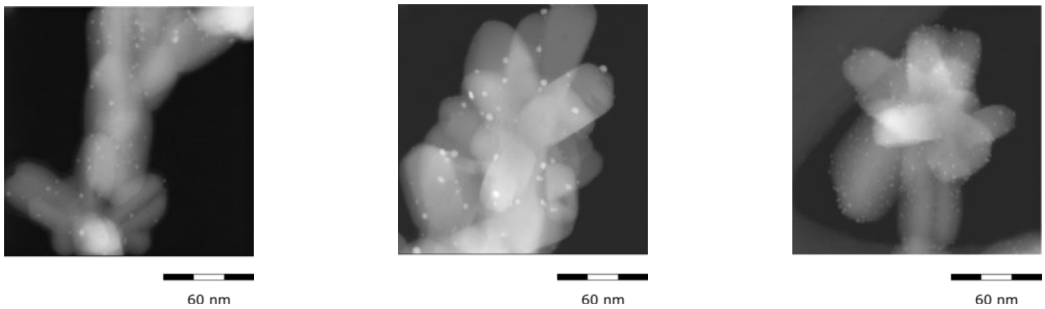

Fig. 7. Representative TEM images of CAT-Pd_1 (a), CAT-Pt_1 (b) and CAT-Pd_2 (c).

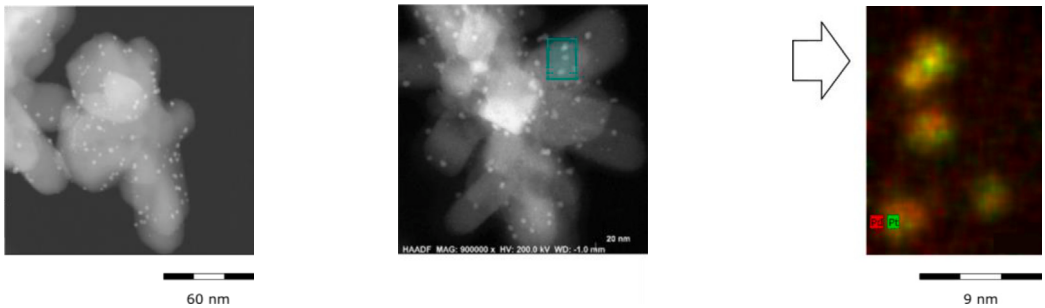

Fig. 8. Representative TEM image of CAT-PdPt_1 (a), TEM image of CAT-PdPt_1 (b) and the corresponding EDXS image (c).

this procedure has been shown in [27] already. The experiments took place at ambient pressure and temperature.

The yellow-coloured complex H_2O_2 and titanium(IV) oxysulfate formed was analysed at a wavelength of 409 nm (5 mm optical quartz glass cuvette (QS, Hellma Analytics), Agilent 8453 UV–vis spectrometer) and the concentration of H_2O_2 was determined from the according calibration.

3. Results and discussion

3.1. Surface morphology

To give a general impression of a catalyst's structure, Fig. 4 shows a SEM image of CAT-Pt_1 in a cross-sectional perspective with a magnification of one hundred times as an example. A TiO_2 layer thickness of 60 µm is estimated from the sectional view of the sample. It can be seen that the main layer is evenly distributed on the surface of the stainless steel surface. Due to the chosen laser scanning strategy in the manufacturing process of the stainless steel structure, unmolten particles remain inside the dense outer contour walls of the wall of the structure. Fig. 5 shows the respective SEM images at the positions of the conducted WDX analyses of the different samples. The main layer volume is made up by TiO_2, as the WDX analyses in Fig. 6 indicate. The noble metal shows a very homogeneous element distribution in the TiO_2-matrix, see Figs. 6(c) and 6(g). When comparing the WDX images of the samples with different Pd loadings (CAT-Pd_1 and CAT-Pd_2), the higher Pd loading of the layer is clearly visible, compare Figs. 6(c) and 6(o). Examining the distribution of the Pd in the layer of CAT-Pd_2, band structures of the Pd are observable. These are due to the procedure of the deposition process itself: to deposit twice the amount of Pd, the SFRD process had to be conducted twice sequentially. To detect Pt, a higher acceleration voltage is needed. Thus, more energy is sent into the coating layer, leading to the formation of cracks in some cases, which is the reason, why the crack in the WDX results in Figs. 6(e)–6(h) is not visible in the original SEM image of the coating, shown in Fig. 5(b). As can be taken from Figs. 6(k) and 6(l), both metals are evenly distributed in the layer of CAT-PdPt_1.

3.2. Particle size distribution

Fig. 7 represents TEM images of particles which were scraped off CAT-Pd_1, CAT-Pt_1 and CAT-Pd_2, while Fig. 8 shows a representative TEM image of the bimetallic CAT-PdPt_1 and a EDXS image showing the distribution of Pd and Pt nanoparticles.

Figs. 9(a) and 9(b) present the particle size distributions and frequencies for the examined samples with different Pd loadings, derived by image analysis and particle counting. From the data summarised in Table 2 follows that in all experiments very small metallic nanoparticles with a mean diameter in the range from $x_{50,0}$ = 1.8 to 2 nm were produced. However, it must be considered that this difference is within the error limit. It also follows from Table 2 and Figs. 9(c) and 9(d), that for both, Pd and Pt, the same mean particle size of 1.9 nm is obtained. Thus, the difference between the single particle sizes is very small. Furthermore, a narrow particle size distribution from Δ = 0.49 for CAT-PdPt_1, Δ = 0.52 for CAT-Pd_1, to Δ = 0.75 for CAT-Pt_1 was obtained. Surprisingly, an increase of the Pd target loading from 1 to 2 wt.-% results in a slightly smaller, mean particle size (1.8 nm) and the narrowest size distribution (Δ = 0.35). The interpretation of the differences is the subject of ongoing and future investigations. Among others, the differences are most likely caused through the low solubility of $Pd(acac)_2$ in $scCO_2$, compared to the about 30 higher solubility of $Pt(cod)me_2$ and the different adsorption behaviour of the two precursors [25]. Thus, to achieve a target loading of 2 wt.-% Pd requires the subsequent deposition of the precursor.

It is also observed that the PdPt nanoparticles show a bimodal particle size distribution, as can be taken from Figs. 9(e) and 9(f), which show the particle size distribution and frequency of the sample with substrate CAT-PdPt_1.

3.3. Productivity

Fig. 10(a) shows the productivities calculated from the measured concentrations of H_2O_2 for the catalysts with different types of metal

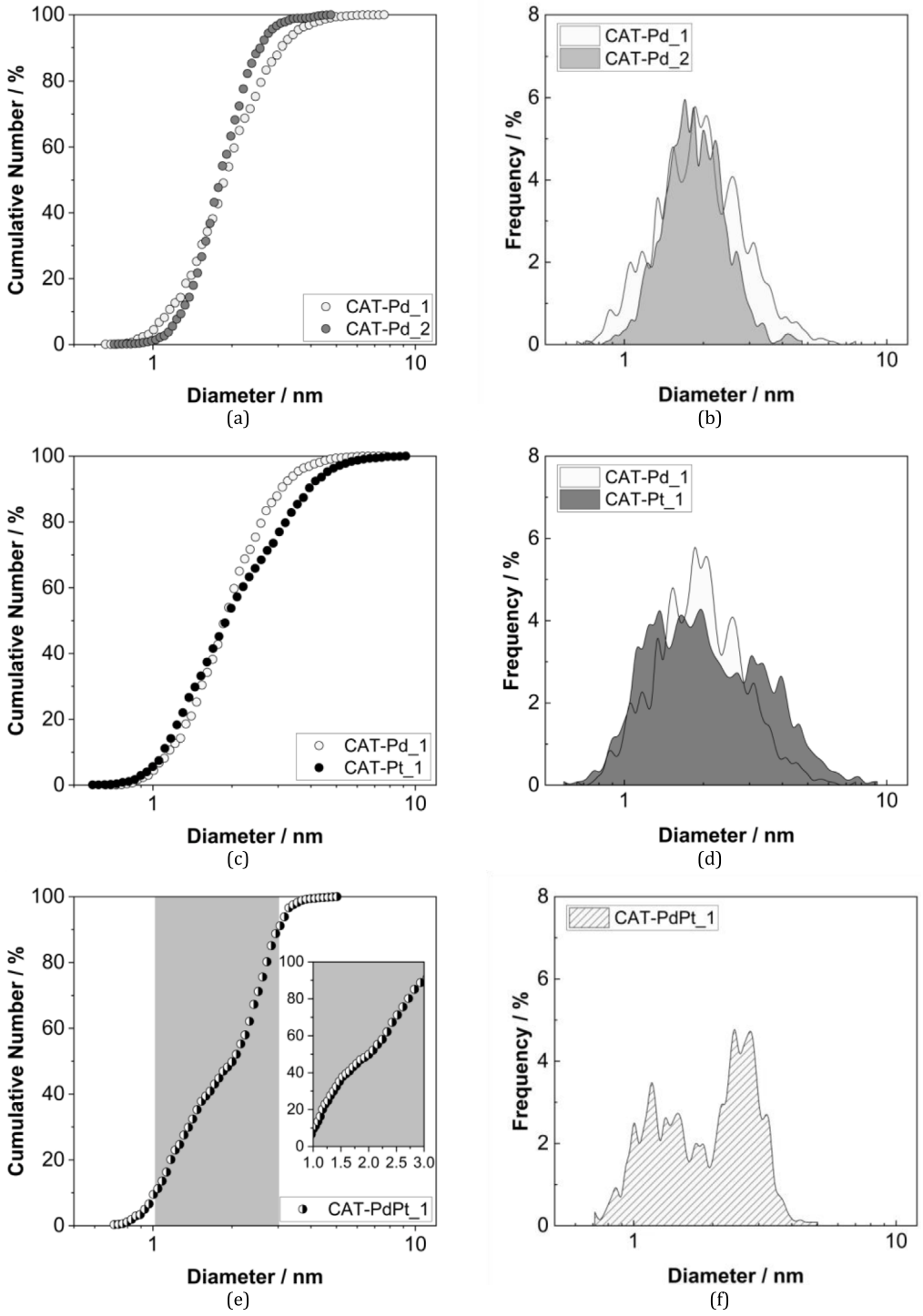

Fig. 9. Particle size distribution and frequency of CAT-Pd_1 and CAT-Pd_2 (a) and (b), of CAT-Pd_1 and CAT-Pt_1 (c) and (d) and CAT-PdPt_1 (e) and (f), derived from TEM images.

(CAT-Pd_1, CAT-PdPt_1 and CAT-Pt_1) over the time of the experimental run, whereas Fig. 10(b) gives the resulting mean productivities. As it can be seen in both graphs, the productivity determined for CAT-Pd_1 lies well above the one of CAT-Pt_1. It has to be noted that a shift in the concentration of Pt towards a fourth or tenth of the Pd loading however might lead to a different picture, as indicated by results presented in [31] for the reaction in a methanol system and in [32] in an ethanol-based medium respectively. However, different support materials were used in both investigations.

The productivity of the bimetallic CAT-PdPt_1 is found to be slightly higher, but almost similar, to the one of the monometallic CAT-Pd_1. Xu et al. observed this trend of increasing productivity in their work on the comparison of the activity of bimetallic PdPt catalysts with different Pd-Pt-loading ratios towards the direct synthesis reaction in ethanol [32]. They suggest that the OH-radical formation, the main responsible intermediate for the water synthesis, is strongly reduced by the alloy, because the dissociative adsorption of oxygen on the surface could be suppressed.

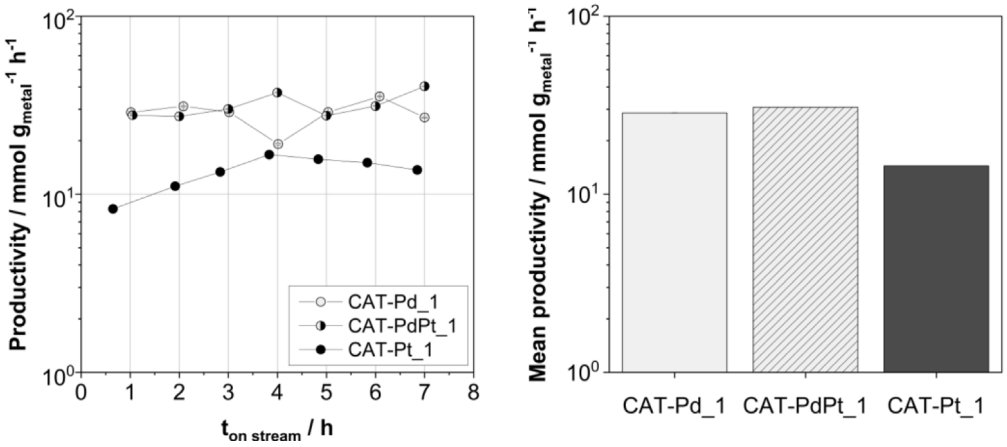

(a) (b)

Fig. 10. Productivities calculated and monitored over time and the derived mean values for the different catalysts evaluated in this work. Comparison of the impact of the noble metal, time-dependent depiction (a) and mean values (b). The corresponding error bars are not visible in (b) due to the scaling of the plot.

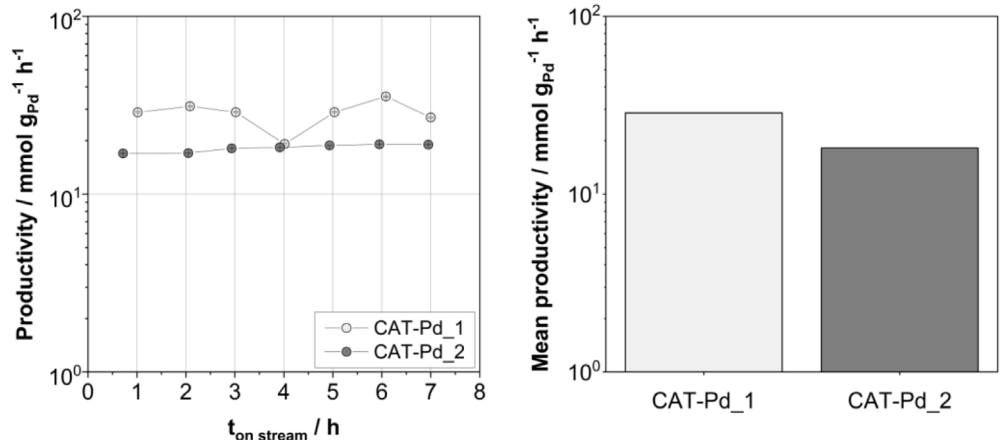

(a) (b)

Fig. 11. Productivities calculated and monitored over time and the derived mean values for the different catalysts evaluated in this work. Comparison of the impact of the metal (Pd) loading, time-dependent depiction (a) and mean values (b). The corresponding error bars are not visible in (b) due to the scaling of the plot.

Table 2
Effect of metal precursor on PSD of mono- and bimetallic metal nanoparticles.

Property	Substrates			
	CAT-Pd_1	CAT-Pt_1	CAT-PdPt_1	CAT-Pd_2
Precursor 1	$Pd(acac)_2$	–	$Pd(acac)_2$	$Pd(acac)_2$
Precursor 2	–	$Pt(cod)me_2$	$Pt(cod)me_2$	–
Metal	Pd	Pt	Pd&Pt	Pd
$x_{10,0}$/nm	1.1	1.1	1.0	1.3
$x_{50,0}$/nm	1.9	1.9	2.0	1.8
$x_{90,0}$/nm	3.1	3.9	3.0	2.6
Δ/–	0.52	0.75	0.49	0.35

$\Delta = (x_{90,0} - x_{10,0})/(2 \cdot x_{50,0})$.

Fig. 11 shows that an increase of the Pd loading from 1 to 2 wt.−% leads to a decrease in the productivity. Contra intuitive at first, however, this is in agreement with findings by [27,33,34]. Though tested in methanol and under elevated pressures, Gemo et al. already reported a decrease of the selectivity of the catalyst with an increase of the Pd loading [33]. In their work on Pd based alloy catalysts, Fu et al. described higher productivities for catalysts with lower Pd loading than for those comparable alloys with higher Pd loading [34].

In Fig. 12 we compare the productivities we determined in this work with the best performing one of the structured catalysts developed by our group in preceding investigations, i.e. the single step deposition of a layer on a substrate with a target loading of 1 wt.-% Pd via a washcoating procedure [27]. It has to be noted at this point, that the catalysts weighed against another are of comparable composition and layer thickness, but that the catalysts themselves are having different morphologic characteristics as the dispersion of the metal component in the TiO_2 or the size of the Pd-cluster. This is due to the precipitation process itself. Nevertheless, it is obvious that the catalyst produced by SFRD presented in this work is leading to a productivity which is outperforming the one achieved with the washcoated sample. These results show, that in case of very small particles, i.e. a mean particle size less or equal 2 nm, the influence of particle size, size distribution, loading and interaction of the different metallic nanoparticles with the surface of the substrate on the catalytic productivity needs to be investigated more detailed. Besides this, there is a need for a deeper understanding about the influence of the various nanoparticle preparation methods on the properties of the produced catalysts.

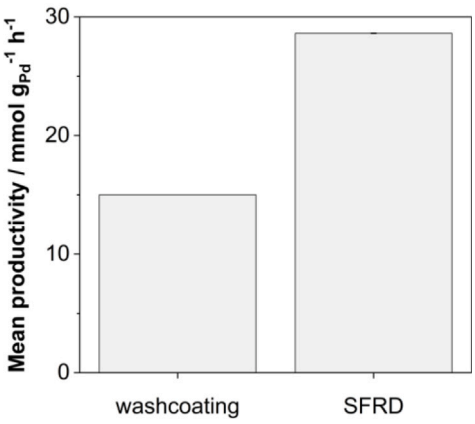

Fig. 12. Comparison of the productivities of FGE with 1 wt.-% Pd on TiO_2-coatings deposited via a washcoating procedure [27] and CAT-Pd_1. Note, to highlight the difference in productivities, the *y*-axis values were plotted linearly. The corresponding error bars are not visible due to the scaling of the plot.

4. Conclusions

Structured catalysts offer a promising frame for heterogeneously catalysed reactions in the liquid phase as the synthesis of H_2O_2 in an aqueous media. We showed that the deposition of homogeneously distributed noble metal nanoparticles on TiO_2-coated, three-dimensional, complex stainless steel structures is possible via the SFRD process. We have conducted experiments using different noble metals by means of SFRD for liquid phase reaction applications, i.e. the direct synthesis of H_2O_2. The comparison of pure Pd, Pt and bimetallic PdPt nanoparticles shows that for the direct synthesis a similarly high productivity is observed for the single Pd and the bimetallic nanoparticles. In addition, an increase in the Pd loading leads to a decrease in the productivity. The comparison with a catalyst prepared by the conventional washcoating method shows that the productivity for the direct synthesis of H_2O_2 is higher for the catalyst prepared via the SFRD method. We thus demonstrated that he reactive deposition of noble metals from supercritical CO_2 is suitable to prepare structured catalysts for the direct synthesis of H_2O_2.

However, for a deeper understanding of the relationship between the process conditions during deposition of the noble metal nanoparticles and the obtained catalytic results it is necessary to gain a more profound insight into the structure, size and size distribution of the noble metal nanoparticles.

CRediT authorship contribution statement

Laura L. Trinkies: Conceptualization, Methodology, Investigation, Catalyst productivity, Data Curation, Writing – original draft, Writing – review & editing, Visualization, Supervision, Project administration. **Marlene Crone:** Investigation, Catalyst metal loading, Data curation, Resources, Writing – review & editing. **Michael Türk:** Methodology, Writing – review & editing, Supervision, Funding acquisition. **Manfred Kraut:** Writing – review & editing, Supervision. **Roland Dittmeyer:** Writing – review & editing, Funding acquisition.

Declaration of competing interest

The authors declare that they have no known competing financial interests or personal relationships that could have appeared to influence the work reported in this paper.

Data availability

Data will be made available on request.

Acknowledgements

The authors would like to thank Heike Störmer (LEM, KIT) for conducting the high precision TEM measurements and Uta Gerhards and Florian Messerschmidt (IMVT, KIT) for SEM, EDX and WDX measurements.

Funding

This work was supported by Deutsche Forschungsgemeinschaft (DFG), Germany through Research Unit 2383 ProMiSe [grant number DI 696/13-2]; the CRC1441 TrackAct (Subproject C1, Project-ID 426888090).

References

[1] J.M. Campos-Martin, G. Blanco-Brieva, J.L.G. Fierro, Hydrogen peroxide synthesis: an outlook beyond the anthraquinone process, Angew. Chem., Int. Ed. Engl 45 (42) (2006) 6962–6984, http://dx.doi.org/10.1002/anie.200503779.

[2] G. McDonnell, The use of hydrogen peroxide for disinfection and sterilization applications, in: Z. Rappoport (Ed.), PATAI's Chemistry of Functional Groups, John Wiley & Sons, Ltd, Chichester, UK, 2009, http://dx.doi.org/10.1002/9780470682531.pat0885.

[3] C.E. Rodriguez-Martinez, M.P. Sossa-Briceño, J.A. Cortés, Decontamination and reuse of N95 filtering facemask respirators: A systematic review of the literature, Am. J. Infect. Control 48 (12) (2020) 1520–1532, http://dx.doi.org/10.1016/j.ajic.2020.07.004.

[4] E.E. Sickbert-Bennett, J.M. Samet, P.W. Clapp, H. Chen, J. Berntsen, K.L. Zeman, H. Tong, D.J. Weber, W.D. Bennett, Filtration efficiency of hospital face mask alternatives available for use during the COVID-19 pandemic, JAMA Intern. Med. 180 (12) (2020) 1607–1612, http://dx.doi.org/10.1001/jamainternmed.2020.4221.

[5] S. Yang, A. Verdaguer-Casadevall, L. Arnarson, L. Silvioli, V. Čolić, R. Frydendal, J. Rossmeisl, I. Chorkendorff, I.E.L. Stephens, Toward the decentralized electrochemical production of H_2O_2: A focus on the catalysis, ACS Catal 8 (5) (2018) 4064–4081, http://dx.doi.org/10.1021/acscatal.8b00217.

[6] Deadly fire and explosions at container depot in Bangladesh: 48 dead and hundreds injured as hydrogen peroxide containers exploded, 2022, Accessed: 23.06.2022, URL https://www.chemistryworld.com/news/deadly-fire-and-explosions-at-container-depot-in-bangladesh/4015799.article.

[7] G. Goor, J. Glenneberg, S. Jacobi, J. Dadabhoy, E. Candido, Hydrogen peroxide, in: Ullmann's Encyclopedia of Industrial Chemistry, Wiley-VCH Verlag GmbH & Co. KGaA, Weinheim, Germany, 2000, pp. 1–40, http://dx.doi.org/10.1002/14356007.a13_443.pub3.

[8] Y. Yi, L. Wang, G. Li, H. Guo, A review on research progress in the direct synthesis of hydrogen peroxide from hydrogen and oxygen: noble-metal catalytic method, fuel-cell method and plasma method, Catal. Sci. Technol. 6 (6) (2016) 1593–1610, http://dx.doi.org/10.1039/C5CY01567G.

[9] C. Samanta, Direct synthesis of hydrogen peroxide from hydrogen and oxygen: An overview of recent developments in the process, Appl. Catal., A 350 (2) (2008) 133–149, http://dx.doi.org/10.1016/j.apcata.2008.07.043.

[10] T. Inoue, K. Ohtaki, S. Murakami, S. Matsumoto, Direct synthesis of hydrogen peroxide based on microreactor technology, Fuel Process. Technol. 108 (2013) 8–11, http://dx.doi.org/10.1016/j.fuproc.2012.04.009.

[11] M. Selinsek, M. Bohrer, B.K. Vankayala, K. Haas-Santo, M. Kraut, R. Dittmeyer, Towards a new membrane micro reactor system for direct synthesis of hydrogen peroxide, Catal. Today 268 (2016) 85–94, http://dx.doi.org/10.1016/j.cattod.2016.02.003.

[12] M. Selinsek, B.J. Deschner, D.E. Doronkin, T.L. Sheppard, J.-D. Grunwaldt, R. Dittmeyer, Revealing structure and mechanism of palladium during direct synthesis of hydrogen peroxide in continuous flow using operando spectroscopy, ACS Catal 8 (3) (2018) 2546–2557, http://dx.doi.org/10.1021/acscatal.7b03514.

[13] M. Selinsek, M. Kraut, R. Dittmeyer, Experimental evaluation of a membrane micro channel reactor for liquid phase direct synthesis of hydrogen peroxide in continuous flow using nafion® membranes for safe utilization of undiluted reactants, Catalysts 8 (11) (2018) 556, http://dx.doi.org/10.3390/catal8110556.

[14] Y. Zhu, B. Bin Mohamad Sultan, X. Nguyen, C. Hornung, Performance study and comparison between catalytic static mixer and packed bed in heterogeneous hydrogenation of vinyl acetate, J. Flow Chem. 11 (3) (2021) 515–523, http://dx.doi.org/10.1007/s41981-021-00152-7.

[15] G.M. Schneider, Physicochemical aspects of fluid extraction, Fluid Phase Equilib. 10 (2–3) (1983) 141–157.

[16] P.F. Siril, M. Türk, Synthesis of metal nanostructures using supercritical carbon dioxide: A green and upscalable process, Small 16 (49) (2020) 2001972, http://dx.doi.org/10.1002/smll.202001972.

[17] G. Brunner, Supercritical process technology related to energy and future directions – An introduction, J. Supercrit. Fluids 96 (2015) 11–20, http://dx.doi.org/10.1016/j.supflu.2014.09.008.

[18] M. Türk, C. Erkey, Synthesis of supported nanoparticles in supercritical fluids by supercritical fluid reactive deposition: Current state, further perspectives and needs, J. Supercrit. Fluids 134 (2018) 176–183, http://dx.doi.org/10.1016/j.supflu.2017.12.010.

[19] C. Erkey, M. Türk, Synthesis of Nanostructured Materials in Near and/Or Supercritical Fluids: Methods, Fundamentals and Modeling, in: Supercritical fluid science and technology, vol. 8, Elsevier, Amsterdam, 2021.

[20] H. Yousefzadeh, I.S. Akgün, S.B. Barim, T.B. Sari, G. Eris, E. Uzunlar, S.E. Bozbag, C. Erkey, Supercritical fluid reactive deposition: A process intensification technique for synthesis of nanostructured materials, Chem. Eng. Process 176 (2022) 108934, http://dx.doi.org/10.1016/j.cep.2022.108934.

[21] C. Erkey, Preparation of metallic supported nanoparticles and films using supercritical fluid deposition, J. Supercrit. Fluids 47 (3) (2009) 517–522, http://dx.doi.org/10.1016/j.supflu.2008.10.019.

[22] M.Z. Özel, M.D. Burford, A.A. Clifford, K.D. Bartle, A. Shadrin, N.G. Smart, N.D. Tinker, Supercritical fluid extraction of cobalt with fluorinated and non-fluorinated β-diketones, Anal. Chim. Acta 346 (1) (1997) 73–80, http://dx.doi.org/10.1016/S0003-2670(97)00159-1.

[23] M. Ashraf-Khorassani, M.T. Combs, L.T. Taylor, Solubility of metal chelates and their extraction from an aqueous environment via supercritical CO_2, Talanta 44 (5) (1997) 755–763, http://dx.doi.org/10.1016/S0039-9140(96)02075-9.

[24] M. Crone, M. Türk, unpublished results, 2023.

[25] M. Türk, M. Crone, G. Upper, Effect of gas pressure on the phase behaviour of organometallic compounds, J. Supercrit. Fluids 58 (1) (2011) 1–6, http://dx.doi.org/10.1016/j.supflu.2011.05.016.

[26] E. Hansjosten, A. Wenka, A. Hensel, W. Benzinger, M. Klumpp, R. Dittmeyer, Custom-designed 3D-printed metallic fluid guiding elements for enhanced heat transfer at low pressure drop, Chem. Eng. Process. 130 (May) (2018) 119–126, http://dx.doi.org/10.1016/j.cep.2018.05.022.

[27] L.L. Trinkies, D. Ng, Z. Xie, C.H. Hornung, M. Kraut, R. Dittmeyer, Direct synthesis of hydrogen peroxide at additively manufactured fluid guiding elements as structured catalysts, Chem. Eng. Process 188 (2023) 109353, http://dx.doi.org/10.1016/j.cep.2023.109353.

[28] Solvay Chemicals, Inc., Solvay chemicals technical publication: H_2O_2 passivation procedure, 2005, accessed: 06.02.2023. URL https://www.solvay.com/sites/g/files/srpend221/files/2019-10/H2O2$%$20Hydrogen$%$20Peroxide$%$20Passivation$%$20Procedure.pdf.

[29] B.J. Deschner, D.E. Doronkin, T.L. Sheppard, G. Rabsch, J.-D. Grunwaldt, R. Dittmeyer, Continuous-flow reactor setup for operando x-ray absorption spectroscopy of high pressure heterogeneous liquid-solid catalytic processes, Rev. Sci. Instrum. 92 (12) (2021) 124101, http://dx.doi.org/10.1063/5.0057011.

[30] A. Pashkova, K. Svajda, G. Black, R. Dittmeyer, Automated system for spectrophotometric detection of liquid phase hydrogen peroxide for concentrations up to 5% w/w, Rev. Sci. Instrum 80 (5) (2009) 055104, http://dx.doi.org/10.1063/1.3120523.

[31] G. Bernardotto, F. Menegazzo, F. Pinna, M. Signoretto, G. Cruciani, G. Strukul, New Pd–Pt and Pd–Au catalysts for an efficient synthesis of H_2O_2 from H_2 and O_2 under very mild conditions, Appl. Catal., A 358 (2) (2009) 129–135, http://dx.doi.org/10.1016/j.apcata.2009.02.010.

[32] J. Xu, L. Ouyang, G.-j. Da, Q.-Q. Song, X.-J. Yang, Y.-F. Han, Pt promotional effects on Pd–Pt alloy catalysts for hydrogen peroxide synthesis directly from hydrogen and oxygen, J. Catal. 285 (1) (2012) 74–82, http://dx.doi.org/10.1016/j.jcat.2011.09.017.

[33] N. Gemo, S. Sterchele, P. Biasi, P. Centomo, P. Canu, M. Zecca, A. Shchukarev, K. Kordás, T.O. Salmi, J.-P. Mikkola, The influence of catalyst amount and Pd loading on the H_2O_2 synthesis from hydrogen and oxygen, Catal. Sci. Technol. 5 (7) (2015) 3545–3555, http://dx.doi.org/10.1039/C5CY00493D.

[34] L. Fu, S. Liu, Y. Deng, H. He, S. Yuan, L. Ouyang, Fabrication of the PdAu surface alloy on an ordered intermetallic Au_2Cu core for direct H_2O_2 synthesis at ambient pressure, Ind. Eng. Chem. Res. 61 (32) (2022) 11655–11665, http://dx.doi.org/10.1021/acs.iecr.2c01482.